FINAL TECHNICAL REPORT FOR THE PROJECT

Plasmonic Control of Radiation and Absorption Processes in Semiconductor Quantum Dots

PI: Roberto Paiella

Department of Electrical and Computer Engineering, Photonics Center, and Division of Materials Science and Engineering, Boston University, 8 St. Mary's Street, Boston, Massachusetts 02215

Phone: 617-353-8883, Email: rpaiella@bu.edu

Co-PI: Theodore D. Moustakas

Department of Electrical and Computer Engineering, Photonics Center, and Division of Materials Science and Engineering, Boston University, 8 St. Mary's Street, Boston, Massachusetts 02215

Phone: 617-353-5431, Email: tdm@bu.edu

Prepared for the U.S. Department of Energy, Office of Science

DOE Award Number: DE-FG02-06ER46332

Award Recipient: Trustees of Boston University

Period Covered: 8/15/2006 – 12/31/2016   Date of Report: March 2017

1. Introduction

This research program has been focused on the control of radiation and absorption processes in semiconductor photonic materials through the use of specially designed metallic nanoparticles (NPs). By virtue of their strongly confined plasmonic resonances [1], these nanostructures can concentrate incident radiation into sub-wavelength "hot spots" of highly enhanced field intensity, thereby increasing optical absorption by suitably positioned absorbers. By reciprocity, the same NPs can also dramatically increase the spontaneous emission rate of radiating dipoles located within their hot spots, in a manner analogous to the Purcell effect in microcavities [2, 3]. Under these conditions, the far-field properties of the emitted light (including polarization and directionality) are then determined by the nature of the NP plasmonic excitations involved in the radiation process, rather than of the original dipole sources. The NPs can therefore be used as optical antennas to enhance the light-emission efficiency of the underlying active material and at the same time control the output radiation far-field pattern.

The study of these phenomena has potentially far-reaching scientific and technological implications. On the one hand, it provides fundamental new understanding of optical processes at the nanoscale, including near-field energy transfer between quantum emitters and photonic nanostructures, dissipation phenomena of plasmonic excitations (i.e., ohmic absorption losses versus scattering), and radiation from nanoantennas. On the other hand, it may pave the way to entirely new device concepts and applications, in a broad range of disciplines including optoelectronics, sensing, spectroscopy, photovoltaics, and even quantum information science (in conjunction with single-photon emitters). A specific application of particularly strong relevance to the DOE mission is the development of energy efficient LED active materials for solid-state lighting, based on plasmonic enhancement effects.

The key accomplishments of the project include the demonstration of highly enhanced light emission efficiency at visible wavelengths using a variety of plasmonic excitations, from propagating surface plasmon polaritons in continuous metal films to localized surface plasmon resonances in metallic NPs, to lattice surface modes in diffractive NP arrays. Using more complex nanostructures, we have also reported the first demonstration of plasmonic unidirectional beaming of luminescence from extended-area incoherent light emitters. Initial results showing the reverse functionality (i.e., plasmonic unidirectional absorption and photodetection) have also been generated with similar systems. Furthermore, we have introduced theoretically a new paradigm for the near-field control of light emission, based on gradient metasurfaces, which may enable unprecedented control of the radiation properties (including efficiency, directionality, and polarization) directly at the source level, without the need for any bulky external optics.

The light emitting materials used in these efforts mostly consist of InGaN/GaN quantum wells grown in the co-PI's lab by plasma-assisted molecular beam epitaxy (MBE). Nitride semiconductors in general provide an ideal solid-state platform for the study of plasmonic control of radiation and absorption processes, because of their widely tunable bandgap energies across the visible spectrum (where the plasmonic resonances of typical metallic nanostructures occur) and favorable near-surface optical properties. Furthermore, they have high technological significance as the leading materials system for solid-state lighting. During the last renewal cycle of the grant, we have also focused on the growth of InGaN quantum dots with high Indium mole fraction, which can allow for the investigation of plasmon enhancement effects at the single-emitter level, as well as enable new applications in photovoltaics. In the course of these activities, we have developed a completely new technique for the synthesis of such quantum dots (droplet heteroepitaxy), with several potential advantages in terms of compositional and geometrical control.

2. Plasmon-enhanced light emission

The basic device geometry used to demonstrate plasmon-enhanced light emission from visible LED materials is shown in Fig. 1(a). In this geometry, the light-emitting dipoles [e.g., excitons in an InGaN/GaN quantum well (QW)] can release their energy through spontaneous emission of radiation, nonradiative decay, or direct near-field excitation of plasmonic oscillations. If the dipoles are located near the NP hot spots (and their emission wavelength is close to a NP plasmonic resonance), the latter process can become the dominant relaxation channel via the aforementioned Purcell enhancement effect. As a result, the overall carrier lifetime is decreased. The energy transferred to the NP plasmonic excitations is then partly dissipated via ohmic absorption losses in the metal and partly scattered into radiation. If the fraction of radiated energy is sufficiently large, the luminescence yield of the combined active-layer/NP-array system can exceed that of the active layer alone, because the deleterious effect of nonradiative decay is effectively mitigated.

This basic idea has been investigated in our lab with various metallic nanostructure geometries, including dispersion-engineered metallo-dielectric multiple layers [4], random arrays of chemically synthesized Ag NPs [5], and square periodic array of Ag nanocylinders fabricated by electron-beam lithography, electron-bean evaporation, and liftoff [6-8]. The largest enhancements in light-emission efficiency were obtained with the latter approach, which is therefore summarized in more detail below.

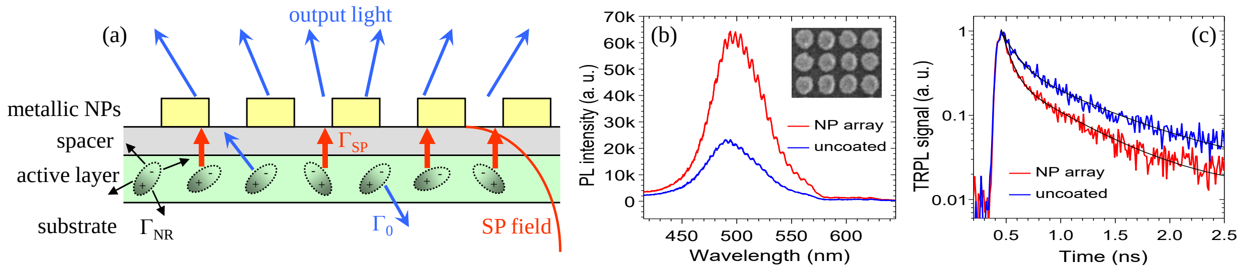

Fig. 1. (a) Schematic illustration of plasmon-enhanced light emission. (b) PL spectra and (c) normalized time-resolved PL (TRPL) signals measured from an uncoated region of an InGaN QW sample (blue lines) and from a region of the same sample under a Ag NP array (red lines). The array [shown in the SEM image in the inset of (b)] has NP diameter *D* = 120 nm, NP height *H* = 55 nm, and period *P* = 160 nm. From [6].

2.1 Localized surface plasmon resonances

A top-view SEM image of a representative device developed in this work is shown in the inset of Fig. 1(b). The Ag NPs in this sample are fabricated directly over the top barrier of an InGaN/GaN multiple-QW active layer emitting around 495 nm (near the technologically important green spectral region). By design, the NPs support localized surface plasmon resonances (LSPRs) at similar wavelengths, as verified via transmission spectroscopy measurements with identical arrays on bulk GaN substrates [6]. Figure 1(b) shows two photoluminescence (PL) spectra measured from an uncoated region of the QW sample (blue line) and from the region underneath the array (red line). Proximity to the NPs clearly results in a substantial increase in PL peak intensity, by a factor of about 2.8 in this case. In Fig. 1(c) the blue and red lines are the normalized time-resolved PL signals measured from the uncoated QWs and from underneath an identical array, respectively. A pronounced decrease in the overall exciton recombination lifetime is observed in going from the bare QWs to the array-coated region, from 123 to 74 ps based on the fitting curves shown in the figure.

These observations are in full agreement with a picture of plasmon-enhanced light emission. Due to the spatial proximity and relatively close spectral match between the QW excitons and the NP LSPRs, efficient recombination via emission of these plasmonic excitations occurs in the sample region below the array, and the PL decay lifetime is correspondingly shortened. As a result, fewer carriers are "wasted" through nonradiative recombination processes, and the spontaneous emission rate and the internal quantum efficiency are correspondingly enhanced (by a factor of over 8 and 5, respectively, based on the detailed analysis of ref. 6). A sufficiently large fraction of the emitted LSPRs are then scattered by the NPs into radiation, leading to an overall increase in PL intensity.

The measured PL-intensity enhancement factors were also found to exhibit a strong dependence on the NP dimensions [6], underscoring the importance of geometrical tuning to engineer these plasmonic interactions. In particular, as the NP diameter *D* is increased the array plasmonic resonance red-shifts away from the QW emission wavelength, and therefore the exciton/LSPR resonant coupling decreases. At the same time, larger NPs generally feature larger scattering efficiency [1], so that more and more of the excited LSPRs are scattered into radiation as opposed to being absorbed in the metal. An optimum value of *D* therefore exists, which in the present case was found to be about 120 nm. Furthermore, the use of taller NPs was shown to provide a more favorable tradeoff between these two conflicting requirements of strong exciton/LSPR coupling and efficient LSPR scattering, consistent with the results of a previous NP-transmission-spectroscopy study carried out under this grant (Fig. 2, [9]). In fact, a monotonic increase in PL-intensity enhancement with increasing NP height *H* (up to about 3.2 for *H* =100 nm) was observed [6].

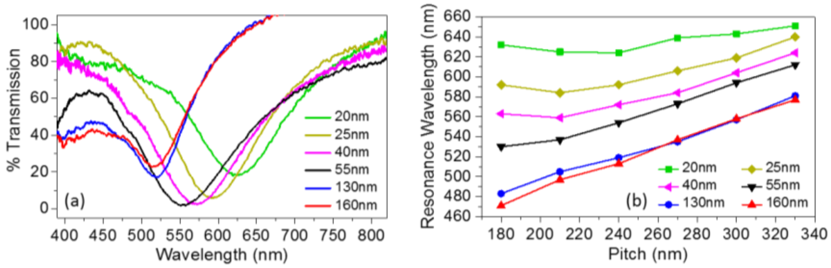

Fig. 2. (a) Measured transmission spectra of Ag NP arrays with 240-nm period and varying NP height (listed in the legend). (b) Plasmonic resonance wavelengths plotted versus array period for different NP heights. The NP diameter is 130 nm in all samples. From [9]. These results show that the plasmonic resonances of NP arrays can be effectively blue-shifted by increasing the NP height. This basic idea has been exploited in ref. 6 to optimize LSPR-enhanced light emission from III-nitride semiconductor QWs at near-green wavelengths, by maximizing the spectral match between the NP LSPRs and the QW excitons, while at the same time benefiting from efficient LSPR scattering in large NPs.

2.2 Lattice surface modes

In subsequent work, we have demonstrated even larger enhancements through the use of lattice surface modes (LSMs) in diffractive NP arrays [8]. These arrays feature periods *P* comparable to or larger than the QW emission wavelength in the semiconductor λ_{em}, so that strong diffraction of the emitted light can occur. In particular, when $P \approx \lambda_{em}$ some of the first-order diffracted light can radiate at grazing angles (i.e., in the plane of the array). As a result, large plasmonic oscillations can be excited in each NP by the in-phase addition of the incident light (the QW luminescence) and the light diffracted by all the other NPs in the array. This phenomenon produces strong LSM resonances of mixed plasmonic and photonic character [10, 11], which can be expected to be particularly favorable in the context of enhanced light emission due to their large scattering efficiency and extended nature across the plane of the QWs.

Experimental results supporting this expectation are shown in Fig. 3(a), where the red lines are the PL spectra measured with five arrays of equal NP height *H* (55 nm) and equal nearest-neighbor spacing *S* (40 nm), but different periods P in the range of 190 to 340 nm. The blue lines are simultaneously measured emission spectra from nearby uncoated regions of the same sample. As shown in the figure, the plasmon-enhanced PL intensity is largest in arrays with period of about 220-240 nm, close to the QW peak emission wavelength in the semiconductor (215 nm, based on an estimated refractive index of 2.3). In these arrays, grazing diffraction of the emitted light becomes allowed so that LSM resonances are supported. The corresponding increase in peak emission relative to the uncoated-QW case is 4.8×, which is substantially larger than the enhancement values obtained with the LSPRs of the previous section.

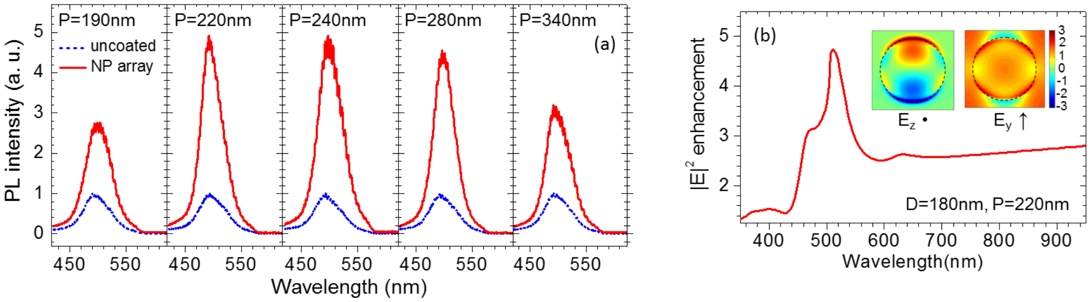

Fig. 3. (a) PL spectra measured with NP arrays of varying period P (red lines), and from nearby uncoated regions of the same sample (blue lines). (b) Spatially averaged electric-field-intensity enhancement spectrum produced in the QWs by the array of (a) with P = 220 nm, under plane-wave illumination at normal incidence. Insets: in-plane (y) and out-of-plane (z) electric-field components at the wavelength of maximum enhancement, plotted in the plane of the QWs within a unit cell of the array. The dashed circles show the NP outline. From [8]

The key role played by LSMs in the arrays of Fig. 3(a) is further confirmed via numerical simulations based on the finite difference time domain (FDTD) method. In particular, we find that the electric-field-intensity enhancement spectrum produced by the NPs in the plane of the QWs is dominated by a strong peak at the LSM resonance wavelength [e.g., about 510 nm in free space for P = 220 nm, as shown in Fig. 3(b)]. Importantly, these resonances are obtained with significantly larger NP diameters D [e.g., 180 nm in Fig. 3(b)] compared to LSPRs at similar wavelengths, which is desirable because of the increase in NP scattering efficiency with increasing diameter. Furthermore, the electric-field distributions associated with LSMs are relatively delocalized on the plane of the QWs [as illustrated in the inset of Fig. 3(b)], so that a large fraction of the light-emitting excitons can couple to these modes. These two properties explain the particularly large PL-intensity enhancements observed in Fig. 3(a). It should be noted that such enhancements of up to 4.8× are quite significant, given the reasonably high (nearly 10 %) internal quantum efficiency of the QWs used in these experiments.

3. Plasmonic unidirectional beaming of luminescence

Under conditions of plasmon-enhanced light emission, as just described, the output light mostly originates from the radiative decay of the excited plasmonic oscillations. As a result, its far-field properties (including directionality and polarization) can be engineered through the design of the metallic nanoantennas supporting these plasmonic resonances. Based on this idea, we have reported the first demonstration of unidirectional light emission along geometrically tunable angles from an extended-area ensemble of incoherent dipole sources [12].

This work is based on the general device geometry shown in Fig. 4(a), consisting of an ultrathin Ag film coated with a periodic array of Ag NPs (possibly with a dielectric spacer layer in between). Due to its ultrasmall thickness (a few 10 nm), the Ag film supports hybrid surface plasmon polaritons (SPPs) extending over both its bottom and top surfaces, as illustrated by the red and black lines in Fig. 4(a). These hybrid SPPs feature complex and geometrically tunable dispersion properties, which have also been investigated in detail in this project [13], as illustrated in Fig. 4(b). For the demonstration of plasmonic beaming, the ultrathin Ag film supporting the NP array is deposited over a light emitting active layer (again consisting of InGaN/GaN QWs emitting near 500 nm). In this geometry, most excitons in the QWs recombine through the near-field excitation of the hybrid SPPs of Fig. 4(a), because of the Purcell enhancement effect discussed previously. Efficient light emission across the film can then occur through the diffractive scattering of the excited SPPs by the overlaying NP array. As a result, the far-field pattern of the emitted light can be tailored by controlling the NP shape and spatial distribution.

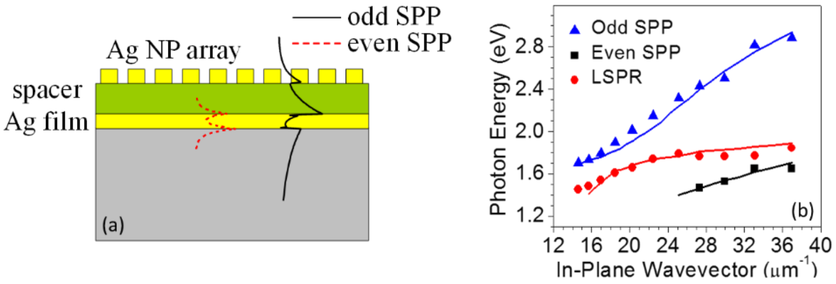

Fig. 4. (a) Schematic cross section of the basic device geometry used to demonstrate plasmonic collimation and beaming. (b) Plasmonic dispersion curves of a device based on the structure of (a), obtained via transmission spectroscopy measurements for different array periods. The two anticrossing gaps observed in this figure can be tuned by varying the thicknesses of the Ag film and of the overlaying dielectric (ZnS) spacer. From [13].

In particular, light produced via diffractive scattering of these hybrid SPPs emerges from the sample surface at an angle θ [Fig. 5(a)] which is determined by the diffraction condition $2\pi\sin\theta/\lambda_0 = k_{SPP} - 2q\pi/\Lambda$, where λ_0 is the wavelength, Λ the array period, q the diffraction order, and $k_{SPP} = 2\pi/\lambda_{SPP}$ the SPP wavenumber. If the array consists of a simple one-dimensional grating of *y*-oriented rectangular ridges [as in Fig. 5(b)], first-order diffraction of forward and backward travelling SPPs (along the *x* direction) leads to the emission of two output beams along equal and opposite angles $\pm\theta$ (on the *x-z* plane). Unidirectional light emission (again on the *x-z* plane) can then be obtained using asymmetric grating lines, designed to suppress diffractive scattering of forward traveling SPPs in favor of backward diffraction (or vice versa). The geometry used in this work consists of lines of triangular NPs, as shown in the schematic picture of Fig. 5(c) and in the top-view SEM image of Fig. 5(d).

The behavior just described is clearly observed in the measured far-field radiation patterns shown in the polar plots of Figs. 5(e)-(g) (i.e., normalized output intensity I versus emission angle θ on the *x-z* plane). In all samples, the output light is found to be predominantly *p*-polarized (consistent with the polarization properties of the SPPs involved in the emission process), and therefore only *p*-polarized data are shown in these figures. The red trace of Fig. 5(e) corresponds to a 1D grating of rectangular ridges with period Λ = 400 nm (close to the expected SPP wavelength λ_{SPP}, so that the first-order diffraction condition is satisfied for $\theta = 0°$). Strong collimation along the sample surface normal is correspondingly obtained, with divergence angle as small as 12° (full width at half maximum). By comparison, an approximately Lambertian profile with large (> 110°) divergence is measured from the same light-emitting samples without any metallic coating, as shown by the blue trace in the same plot. At larger grating periods Λ, the far-field pattern consists of two output beams propagating along equal and opposite angles $\pm\theta$, as illustrated in Fig. 5(f).

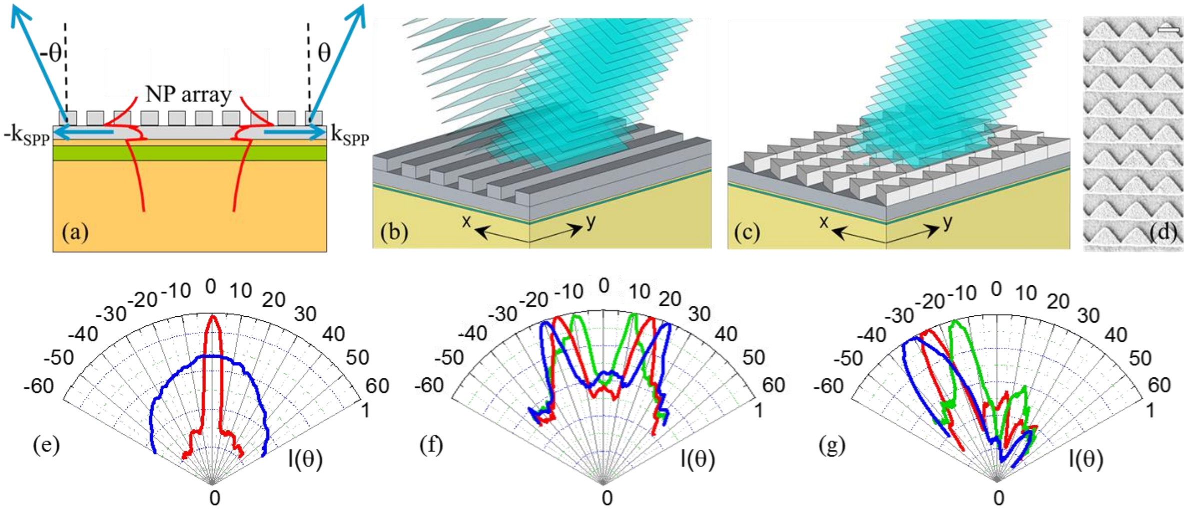

Fig. 5. (a) Schematic cross section of the device geometry of ref. 12 [similar to Fig. 4(a) but without the spacer between the Ag film and the NP array]. The green region indicates the active layer. (b) Grating array designed to emit light along two equal and opposite directions. (c) Triangular NP array designed to emit light along a single off-axis direction. (d) SEM image of a triangular NP array. The scale bar is 500 nm. (e) Experimental *p*-polarized far-field radiation patterns measured with a 1D grating of period $\Lambda = \lambda_{SPP}$ (red trace) and with an otherwise identical uncoated sample (blue trace, normalized to the peak value of the red trace). (f) Radiation patterns measured with 1D gratings of different periods $\Lambda > \lambda_{SPP}$. (g) Radiation patterns measured with different arrays of triangular NPs. All traces in (f) and (g) are normalized to unit peak values. From [12].

Finally, the traces of Fig. 5(g) correspond to the triangular-NP geometry of Fig. 5(c) for different values of the array period and NP size. In this case, off-axis unidirectional beaming is obtained, with most of the output light emitted in a single beam at a nonzero angle with respect to the sample surface normal. The beaming angle can be tuned by varying the array geometrical parameters, as illustrated in the figure. These experimental observations are also well reproduced by FDTD simulations based on the principle of reciprocity [12]. Altogether they represent a novel functionality with considerable technological potential in the context of highly integrated optoelectronic systems (e.g., involving arrays of light-emitting devices), which are often limited by the need for bulky external optical elements to collect and collimate the output light.

4. Metasurface-enhanced light emission

More recently, we have introduced a powerful generalization of the notion of plasmon-enhanced light emission based on the use of gradient metasurfaces (GMSs) [14]. These structures have emerged recently from extensive research in nanophotonics as a useful new tool for the control of externally incident optical wavefronts [15, 16]. In their simplest form, they consists of a planar array of nanoantennas with subwavelength separation and spatially varying shape, size, and/or orientation, designed to introduce a linearly graded phase shift in the light reflected from and/or transmitted through the array. As a result, incident light of in-plane wavevector **p** is scattered by the GMS into a reflected and/or transmitted wave of in-plane wavevector $\mathbf{p} + \hat{\mathbf{u}}\xi$, where $\hat{\mathbf{u}}$ and ξ are the direction and magnitude of the phase gradient, respectively. At the same time, all other orders of diffraction are in principle completely suppressed. In recent years, this property has been exploited to demonstrate a wide range of functionalities, including anomalous reflection and refraction, light focusing in ultrathin lenses, generation of optical vortices, and the photonic spin Hall effect (as reviewed, e.g., in refs. 15 and 16).

In the work of ref. 14, we have investigated the radiation properties of an arbitrary light source located in the near-field zone of a reflective GMS, using general theoretical considerations supported by rigorous FDTD simulations. To cover the most general possible situation, we have used the homogenized continuum model shown schematically in Fig. 6(a), which can be applied to any (reflective) GMS regardless of the specific design of the NP array [17]. In this model, the GMS is described as a perfect electric conductor (PEC) coated with an ultrathin metamaterial slab, where the permittivity ε and permeability μ vary linearly with position along the *x* direction. As a result, a position-dependent reflection phase shift $\Phi_{\mathrm{GMS}} = \Phi_0 + \xi x$ is obtained (where Φ_0 is a constant phase). The GMS absorption losses are also included in the model through an imaginary term κ in ε and μ, whose value was selected based on the experimental report of anomalous reflection from a GMS at visible wavelengths [18]. Finally, the light source in Fig. 6(a) is provided by a simple oscillating electric dipole, as appropriate to the description of spontaneous emission in typical luminescent media.

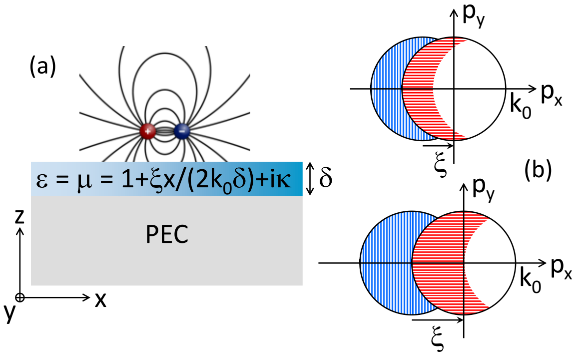

Fig. 6. Light emission near a reflective GMS with linear phase profile. (a) Schematic cross-sectional view of the model system used in this study. (b) Distribution of the plane-wave components of the dipole field involved in the main radiation process, for two different values of the normalized phase gradient ξ/k_0 (0.6 in the upper plot and 1.0 in the lower plot).

The effect of the GMS in this geometry can be understood by first decomposing the optical field emitted by the dipole in a superposition of plane waves with all possible in-plane wavevectors **p** (including evanescent terms with $p > k_0 = 2\pi/\lambda_0$). As already mentioned, at the GMS each such wave produces a reflected wave of in-plane wavevector $\mathbf{p}+\hat{\mathbf{x}}\xi$. As a result, some of the evanescent components of the dipole field can be scattered by the GMS into propagating waves, and therefore contribute to the radiation output. This process is illustrated schematically in Fig. 6(b) for two values of the normalized phase gradient ξ/k_0. In these plots, the blue region of the p_x-p_y plane is the set of all evanescent components that can be scattered by the GMS into radiation, and the resulting propagating waves are contained in the red region. Since this radiation mechanism is mediated by near-field interactions involving highly confined evanescent fields, it can be expected to occur with high probability and thus dominate the dipole emission. Under these conditions, the far-field radiation pattern will mostly consist of plane-wave components from within the red region of Fig. 6(b), leading to directional emission.

These expectations are confirmed by the FDTD simulation results summarized in Fig. 7, computed at a representative visible wavelength λ_0 of 800 nm for a dipole at a distance of 8 nm from the GMS. The color maps of Figs. 7(a)-(c) show the calculated far-field radiation patterns for different values of ξ/k_0. Highly asymmetric directional emission is clearly observed, with the angle of peak emission depending on ξ/k_0 as predicted by the qualitative picture just presented. At the same time, the spontaneous emission decay of the dipole is greatly accelerated by the GMS, again through the excitation of the evanescent components from the blue region of Fig. 6(b). The resulting Purcell enhancement factor F_p (i.e., the spontaneous emission rate near the GMS normalized to that of an identical dipole in free space) ranges from a few 10s to several 100s, depending on ξ/k_0 and on the dipole orientation, as shown in Fig. 7(d). Particularly large values of F_p are obtained for $\xi/k_0 \approx 2$, where the number of evanescent components that can be scattered into radiation is maximized.

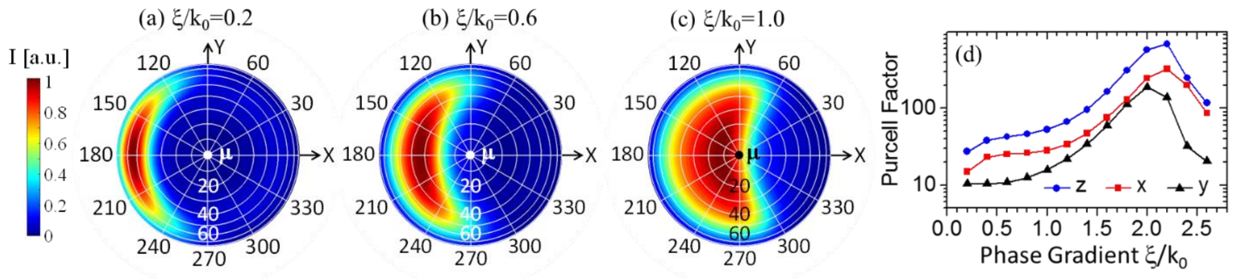

Fig. 7. Simulation results for the geometry of Fig. 6. (a)-(c) Far-field radiation patterns produced by a z-oriented dipole near a GMS with normalized phase gradient ξ/k_0 = 0.2 (a), 0.6 (b), and 1.0 (c). (d) Purcell enhancement factor of a dipole oriented along the x, y, or z directions plotted as a function of ξ/k_0. In all plots, the dipole radiation wavelength λ_0 is 800 nm, and its distance d from the GMS is equal to $\xi/100$. The x, y, and z directions are as defined in Fig. 6(a). From [14].

If the dipole source has an internal quantum efficiency (IQE) of less than about 10%, this accelerated emission rate can also lead to an increase in the total output radiation power (integrated over all directions) [14], similar to the case of plasmon-enhanced light emission described above. Vice versa, for a dipole with larger IQE, the total output power is decreased (by a factor of less than about 10× for $\xi/k_0 < 1$), mostly because some of the dipole emission is captured by the GMS via scattering into surface waves. The latter behavior is also directional, with the excited surface waves predominantly propagating along the positive x direction [14], which may find interesting future applications in nanoscale photonic integrated circuits.

Importantly, all the phenomena just described could not be explained simply in terms of anomalous reflection by the GMS of externally incident radiation from a distant dipole (in fact, nearly opposite radiation patterns would be obtained in that case). Instead, they highlight a unique near-field behavior of GMSs, related to the strong coupling between evanescent and propagating waves enabled by their phase gradient. The resulting ability to tailor the light output directly at the source level (without the need for any bulky external optics) is technologically significant for the continued miniaturization of optical components, and could be extended to other radiation mechanisms such as involving nonlinear optical processes. More advanced beam shaping functionalities via similar near-field interactions (including polarization control and the generation of light with orbital angular momentum) can also be envisioned with GMS phase profiles of increased complexity.

5. Plasmonic unidirectional absorption and photodetection

The basic ideas presented in the last two sections have also been investigated for the demonstration of directional light absorption and photodetection. Specifically, if the nanostructures of Fig. 5 are fabricated on a photoconductive layer and illuminated from the top side, photodetection could only take place through an indirect process where the incident light is first diffracted by the NP array into SPPs supported by both surfaces of the metal film. As these guided waves propagate along the film, they can then be absorbed through the creation of photocarriers in the underlying active layer. Because of the diffraction condition, only light incident along specific directions [again determined by the equation $2\pi\sin\theta/\lambda_0 = k_{SPP} - 2q\pi/\Lambda$] can be efficiently coupled into SPPs and therefore photodetected, depending on the array period Λ. To enable the selective detection of only one incident direction, we can then use asymmetric grating lines such as the triangular NPs of Fig. 5(c) or suitably designed GMSs.

Recently, we have investigated the development of nanostructures specifically designed to implement this novel functionality, including the use of slits in the metal film to enhance the coupling between SPPs at the upper and lower surfaces. FDTD simulation results are shown in Fig. 8(a), where we plot the power transmission coefficient for *p*-polarized incident light through several optimized metasurfaces of different period, as a function of the polar angle of incidence θ. If the same metasurfaces are fabricated on a photodetector active material, the detected signal would be proportional to this transmission coefficient. As shown in the figure, such devices can provide tunable directional photodetection, with a wide tuning range for the angle of peak transmission θ_{max} of ±75° and relatively narrow angular resolution, ranging from 6° to 18° full-width-at-half-maximum as θ_{max} is increased. The peak transmission is in the range of 30-45 % for all designs considered, which is quite reasonable.

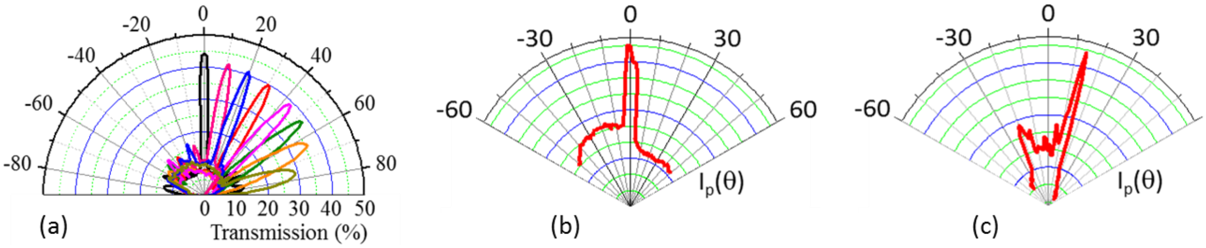

Fig. 8. (a) Calculated power transmission coefficient of *p*-polarized light through several metasurfaces designed for unidirectional photodetection, plotted versus polar angle of incidence θ. (b, c) Measured photocurrent versus polar angle of incidence for two devices based on a Ge photoconductor coated with different metasurfaces.

Initial experimental results are shown in Figs. 8(b) and 8(c), where we plot the measured photocurrent signal versus polar angle of incidence θ for two different structures fabricated on a Ge photoconductor, illuminated with *p*-polarized light at 1550-nm wavelength. Highly directional photodetection is clearly observed in both plots, along the sample surface normal in Fig. 8(b) and near θ = 14° in Fig. 8(c), in good agreement with the designed angles of peak transmission for the respective metasurfaces. While additional work is needed to optimize the device fabrication, these initial results are very promising and further underscore the unique flexibility offered by plasmonic nanostructures to control light-matter interaction.

It should also be noted that these devices are functionally analogous to the individual elements (ommatidia) of compound eyes, which represent the most prevalent vision modality in nature. Therefore, this research may lead to development of image sensors with the unique attributes of compound-eye vision (including large fields of view, nearly infinite depth of focus, and high acuity to motion), but in a flat ultrathin and lens-free package.

6. Semiconductor quantum-well and quantum-dot materials development

The semiconductor active materials used in this project mostly consist of III-nitride quantum structures synthesized in the co-PI's lab by plasma-assisted molecular beam epitaxy (MBE). In particular, the experimental demonstrations of plasmon-enhanced light emission and unidirectional beaming reviewed in sections 2 and 3 were based on high-quality InGaN/GaN multiple-QW samples. In order to improve the radiative properties and extend the spectral range of these active layers, in the course of the same materials development efforts we have also investigated the growth of single-atomic-layer InN QWs [19, 20]. While the resulting samples have not yet been used in conjunction with plasmonic nanostructures, recent transport studies carried out by collaborators have revealed interesting physical properties of the underlying two-dimensional electron gas, including evidence for topological-insulator behavior [20].

More recently, our materials development efforts have focused on the growth of InGaN quantum dots (QDs) with high Indium mole fraction. Such QDs are particularly interesting in the context of this project due to their highly localized nanoscale geometry, which could allow to directly probe the giant optical-field enhancements produced by metallic NPs in their hot spots. Furthermore, high-In-content InGaN QDs are uniquely promising for the demonstration of high-efficiency photovoltaic energy conversion based on the intermediate-band device concept [21] – a potentially transformative application that could also benefit strongly from the use of plasmonic enhancement effects. Two synthesis methods have been pursued for the development of high-quality QD samples: (a) the traditional method of epitaxial self-assembly using the Stranski-Krastanov (SK) growth mode and (b) a brand new technique based on droplet heteroepitaxy [22].

6.1 Stranski-Krastanov method

The SK growth mode relies upon accumulated in-plane compressive strain in order to induce a transition from 2D to 3D growth. Using this method we have investigated the growth and characterization of InGaN QD structures on (0001) GaN templates. A few monolayers of InGaN are deposited at 440 °C followed by annealing at 520 °C. During this annealing step we observe that the RHEED pattern converts from relatively streaky to spotty, indicating a transition from 2D to 3D surface morphology [inset of Fig. 9(a)]. We have also observed that doping the InGaN with Si facilitates this transition, a result attributed to the antisurfactant nature of Si. Figure 9(a) contains a 1µm × 1µm AFM image showing InGaN QDs formed by this method with density of about ~10^{11} cm^{-2} and average height of about 1.5 nm. An In content of 30% could be obtained with these QDs, as determined by x-ray diffraction (XRD).

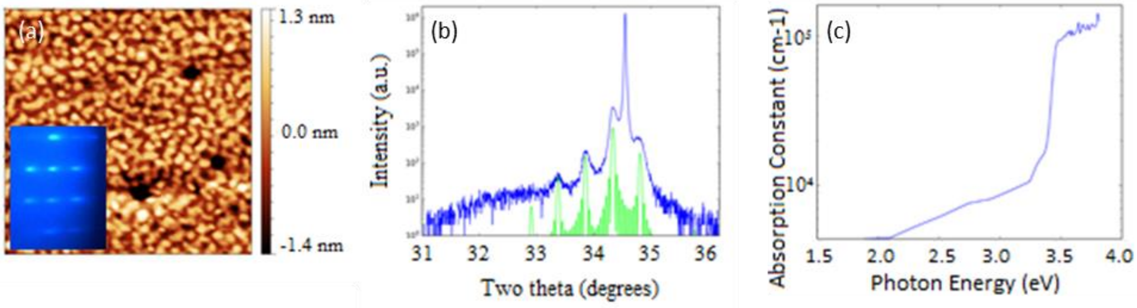

Fig. 9. (a) 1µm × 1µm AFM image of the synthesized InGaN QDs. The inset shows the RHEED pattern along the [11-20] azimuth. (b) XRD data from a multiple-QD sample consisting of 10 InGaN/GaN stacks. (c) Absorption spectrum of an InGaN/GaN multiple-QD sample grown on a thick GaN template.

Samples containing multiple layers of InGaN/GaN QDs have also been formed by the SK method. Figure 9(b) shows the XRD scan from a multiple QD sample consisting of 10 InGaN/GaN layers, indicating good periodicity of the whole structure. Figure 9(c) shows the optical absorption coefficient versus photon energy for a multiple-QD sample consisting of 4 InGaN/GaN stacks. These data clearly show the energy gap of the GaN template occurring approximately at 3.4 eV. The absorption tail extending through the visible spectrum is due to the InGaN QDs. P-I-N junctions with the P-and N-layers consisting of GaN and the I-layer consisting of InGaN/GaN multiple-QDs have also been grown and characterized, showing excellent rectification properties. This result in conjunction with the absorption data of Fig. 9(c) suggests the strong potential of such structures for photovoltaics.

However, the SK method by nature has a number of limitations, since there is an optimum amount of strain required for the formation of QDs, and therefore it is impossible to decouple wetting layer thickness, QD composition, QD dimensions, and template material from one another. Due to these limitations, growth of InGaN QDs on GaN templates by this method has been limited to a narrow range of alloy compositions. Also, the presence of the wetting layer complicates the electronic structure of the combined wetting layer/QD system.

6.2 Droplet heteroepitaxy

In-Ga mixtures are thermodynamically stable in the entire compositional range at relatively low temperatures [23]. Thus, the novel method of droplet heteroepitaxy, which has not been investigated previously, has the potential to form InGaN QDs in the entire alloy composition without a wetting layer by exposure to active nitrogen of liquid In-Ga droplets formed on a substrate. The nucleation of the In-Ga liquid film on the substrate is governed by the interfacial free energy between the liquid deposit and the substrate σ_{ds}, between the liquid deposit and the vapor σ_{dv}, and between the vapor and the substrate σ_{vs}. At equilibrium the liquid deposit forms a hemispherical cap on the top of the substrate and the contact angle θ is given by the expression $\cos\theta = (\sigma_{vs}-\sigma_{sd})/\sigma_{dv}$. If $\sigma_{vs}-\sigma_{sd} = \sigma_{dv}$ then $\theta=0$ and the deposit is said to wet the substrate and forms a continuous liquid film. If on the other hand $\sigma_{vs}-\sigma_{sd} < \sigma_{dv}$ then the In-Ga solution forms liquid droplets.

After the formation of such In-Ga liquid nano-droplets, active nitrogen (N, N^+, N_2^*) produced in an RF plasma source is used to convert the droplets into InGaN QDs. The growth parameter space includes the In/(In+Ga) flux ratio, the total metal flux, the number of monolayers deposited, the deposition temperatures, annealing and nitridation, and the flux and nature of the nitrogen species.

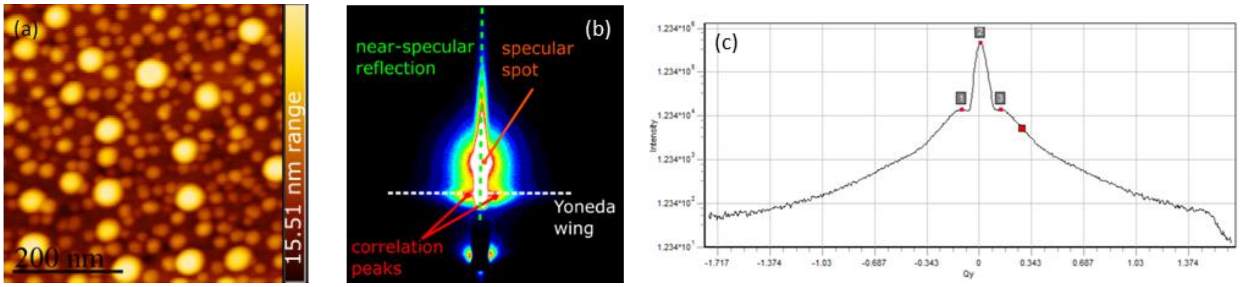

Fig. 10. (a) AFM image of single layer InGaN QDs formed by droplet heteroepitaxy. (b) GISAXS pattern of another sample synthesized by the same method. (c) Intensity plot along the Yoneda wing from the pattern of (b).

InGaN QDs formed by this method were characterized by a number of structural techniques, such as RHEED, AFM, FESEM, GISAXS, TEM, and STEM, to determine their geometrical and microstructural properties. Figure 10(a) is a typical example of an AFM image of such InGaN QDs, in which the In-Ga droplets were deposited and crystallized into dots at 300 °C. The observed bimodal distribution of the QDs was found to depend sensitively on the total In+Ga flux as well as the growth temperature. Specifically higher temperatures promote the formation of larger dots at reduced areal density. The nitridation temperature was also found to affect the crystal structure of the dots, with zincblende dominating at low temperatures and wurtzite at higher temperatures. Composition maps by EDX in STEM indicate inhomogeneities attributed to compositional pulling and localized strain fields.

We have also developed the capability for in-house lab-scale grazing incidence small angle x-ray scattering (GISAXS) characterization of single- and multi-layer QD samples [22]. This method enables effective determination of parameters such as dimensions, shape, lateral and vertical correlation, and areal density. Figure 10(b) shows the GISAXS pattern for one of the samples with annotated descriptions of the various features, and the extracted intensity vs q_y plot is shown in Fig. 10(c). The correlation length and areal density were determined from the analysis of horizontal slices of the GISAXS patterns along the

Yoneda wing shown in Fig. 10(b). The size and shape of the QDs were obtained by numerical fitting of the GISAXS data with a real-space scattering model. All mean QD shapes were observed to be well described as truncated cones. Several trends were also observed relating the QD geometrical properties to the growth parameters – e.g., the overall size increases with nitridation temperature and decreases with nominal InN mole fraction.

While further work is needed to optimize the growth process, these results already support the feasibility of this novel method of III-nitride QD synthesis, which can provide unmatched flexibility in terms of accessible alloy compositions and control of the QD geometrical properties.

7. References

[1] S. A. Maier, *Plasmonics: Fundamentals and Applications* (Springer, 2007).

[2] E. M. Purcell, “Spontaneous emission probabilities at radio frequencies,” *Phys. Rev.* **69**, 681 (1946).

[3] W. L. Barnes, “Fluorescence near interfaces: the role of photonic mode density,” *J. Mod. Opt.* **45**, 661 (1998).

[4] J. Henson, A. Bhattacharyya, T. D. Moustakas, and R. Paiella, “Controlling the recombination rate of semiconductor active layers via coupling to dispersion-engineered surface plasmons,” *J. Opt. Soc. Am. B* **25**, 1328 (2008).

[5] J. Henson, J. C. Heckel, E. Dimakis, J. Abell, A. Bhattacharyya, G. Chumanov, T. D. Moustakas, and R. Paiella, “Plasmon enhanced light emission from InGaN quantum wells via coupling to chemically synthesized silver nanoparticles,” *Appl. Phys. Lett.* **95**, 151109 (2009).

[6] J. Henson, E. Dimakis, J. DiMaria, R. Li, S. Minissale, L. Dal Negro, T. D. Moustakas, and R. Paiella, “Enhanced near-green light emission from InGaN quantum wells by use of tunable plasmonic resonances in silver nanoparticle arrays,” *Opt. Express* **18**, 21322 (2010).

[7] R. Paiella, J. Henson, J. DiMaria, E. Dimakis, R. Li, S. Minissale, L. Dal Negro, and T. D. Moustakas, “Plasmon-enhanced near-green light emission from InGaN/GaN quantum wells,” 220th ECS Meeting, paper 2084 (**invited**), Boston (MA), Oct 2011; full article published in *ECS Trans.* **41**, 73 (2011).

[8] J. Henson, J. DiMaria, E. Dimakis, T. D. Moustakas, and R. Paiella, “Plasmon-enhanced light emission based on lattice resonances of silver nanocylinder arrays,” *Opt. Lett.* **37**, 79 (2012).

[9] J. Henson, J. DiMaria, and R. Paiella, “Influence of nanoparticle height on plasmonic resonance wavelength and electromagnetic field enhancement in two-dimensional arrays,” *J. Appl. Phys.* **106**, 093111 (2009).

[10] V. G. Kravets, F. Schedin, and A. N. Grigorenko, “Extremely narrow plasmon resonances based on diffraction coupling of localized plasmons in arrays of metallic nanoparticles,” *Phys. Rev. Lett.* **101**, 087403 (2008).

[11] B. Auguié and W. L. Barnes, “Collective resonances in gold nanoparticle arrays,” *Phys. Rev. Lett.* **101**, 143902 (2008).

[12] J. DiMaria, E. Dimakis, T. D. Moustakas, and R. Paiella, “Plasmonic off-axis unidirectional beaming of quantum-well luminescence,” *Appl. Phys. Lett.* **103**, 251108 (2013).

[13] J. DiMaria and R. Paiella, “Plasmonic dispersion engineering of coupled metal nanoparticle-film systems,” *J. Appl. Phys.* **111**, 103102 (2012).

[14] L. C. Kogos and R. Paiella, “Light emission near a gradient metasurface,” *ACS Photon.* **3**, 243 (2016).

[15] A. V. Kildishev, A. Boltasseva, and V. M. Shalaev, “Planar photonics with metasurfaces,” *Science* **339**, 1289 (2013).

[16] N. Yu and F. Capasso, “Flat optics with designer metasurfaces,” *Nature Mater.* **13**, 139 (2014).

[17] S. Sun, Q. He, S. Xiao, Q. Xu, X. Li, and L. Zhou “Gradient-index meta-surfaces as a bridge linking propagating waves and surface waves,” *Nature Mater.* **11,** 426 (2012).

[18] S. Sun, K.-Y. Yang, C.-M. Wang, T.-K. Juan, W. T. Chen, C. Y. Liao, Q. He, S. Xiao, W.-T. Kung, G.-Y. Guo, L. Zhou, and D. P. Tsai “High-efficiency broadband anomalous reflection by gradient meta-surfaces,” *Nano Lett.* **12**, 6223 (2012).

[19] L. Zhou, E. Dimakis, R. Hathwar, T. Aoki, D. J. Smith, T. D. Moustakas, S. M. Goodnick, and M. R. McCartney, “Measurement and effects of polarization fields on one-monolayer-thick InN/GaN multiple quantum wells,” *Phys. Rev. B* **88**, 125310 (2013).

[20] W. Pan, E. Dimakis, G. T. Wang, T. D. Moustakas, and D. C. Tsui, “Two-dimensional electron gas in monolayer InN quantum wells,” *Appl. Phys. Lett.* **105**, 213503 (2014).

[21] A. Luque and A. Martí, “Increasing the efficiency of ideal solar cells by photon induced transitions at intermediate levels,” *Phys. Rev. Lett.* **78,** 5014 (1997).

[22] J. M. Woodward, A. Yu. Nikiforov, K. F. Ludwig, Jr., and T. D. Moustakas, “Analysis of InGaN nanodots grown by droplet heteroepitaxy using grazing incidence small-angle X-ray scattering and electron microscopy,” submitted to *J. Appl. Phys.* (2017).

[23] T. J. Anderson and I. Ansara, “The Ga-In (gallium-indium) system,” *J. Phase Equilibria* **12**, 64 (1991).

8. Publications in which DOE support is acknowledged

Journal articles:

- J. M. Woodward, A. Yu. Nikiforov, K. F. Ludwig, Jr., and T. D. Moustakas, “Analysis of InGaN nanodots grown by droplet heteroepitaxy using grazing incidence small-angle X-ray scattering and electron microscopy,” submitted to J. Appl. Phys. (2017).
- L. C. Kogos and R. Paiella, “Light emission near a gradient metasurface,” ACS Photon. **3**, 243 (2016).
- W. Pan, E. Dimakis, G. T. Wang, T. D. Moustakas, and D. C. Tsui, “Two-dimensional electron gas in monolayer InN quantum wells,” Appl. Phys. Lett. **105**, 213503 (2014).
- J. DiMaria, E. Dimakis, T. D. Moustakas, and R. Paiella, “Plasmonic off-axis unidirectional beaming of quantum-well luminescence,” Appl. Phys. Lett. **103**, 251108 (2013).

- L. Zhou, E. Dimakis, R. Hathwar, T. Aoki, D. J. Smith, T. D. Moustakas, S. M. Goodnick, and M. R. McCartney, "Measurement and effects of polarization fields on one-monolayer-thick InN/GaN multiple quantum wells," Phys. Rev. B **88**, 125310 (2013).

- T. D. Moustakas, "The role of extended defects on the performance of optoelectronic devices in nitride semiconductors," Phys. Status Solidi A **210**, 169 (2013).

- J. DiMaria and R. Paiella, "Plasmonic dispersion engineering of coupled metal nanoparticle-film systems," J. Appl. Phys. **111**, 103102 (2012).

- J. Henson, J. DiMaria, E. Dimakis, T. D. Moustakas, and R. Paiella, "Plasmon-enhanced light emission based on lattice resonances of silver nanocylinder arrays," Opt. Lett. **37**, 79 (2012).

- R. Paiella, J. Henson, J. DiMaria, E. Dimakis, R. Li, S. Minissale, L. Dal Negro, and T. D. Moustakas, "Plasmon-enhanced near-green light emission from InGaN/GaN quantum wells," 220th ECS Meeting, paper 2084 (**invited**), Boston (MA), Oct 2011; full article published in ECS Trans. **41**, 73 (2011).

- J. Henson, E. Dimakis, J. DiMaria, R. Li, S. Minissale, L. Dal Negro, T. D. Moustakas, and R. Paiella, "Enhanced near-green light emission from InGaN quantum wells by use of tunable plasmonic resonances in silver nanoparticle arrays," Opt. Express **18**, 21322 (2010).

- J. Henson, J. DiMaria, and R. Paiella, "Influence of nanoparticle height on plasmonic resonance wavelength and electromagnetic field enhancement in two-dimensional arrays," J. Appl. Phys. **106**, 093111 (2009).

- J. Henson, J. C. Heckel, E. Dimakis, J. Abell, A. Bhattacharyya, G. Chumanov, T. D. Moustakas, and R. Paiella, "Plasmon enhanced light emission from InGaN quantum wells via coupling to chemically synthesized silver nanoparticles," Appl. Phys. Lett. **95**, 151109 (2009).

- J. Henson, A. Bhattacharyya, T. D. Moustakas, and R. Paiella, "Controlling the recombination rate of semiconductor active layers via coupling to dispersion-engineered surface plasmons," J. Opt. Soc. Am. B **25**, 1328 (2008).

Conference proceedings:

- R. Paiella, L. Kogos, and J. DiMaria, "Plasmonic metasurfaces for the near-field directional control of light emission," 7th International Conference on Metamaterials, Photonic Crystals and Plasmonics (META), paper 3A25, Malaga (Spain), July 2016 (**invited**).

- R. Paiella, "Plasmonic control of quantum-well luminescence for enhanced efficiency and beam shaping," 35th Progress in Electromagnetics Research Symposium (PIERS), Guangzhou (China), Aug 2014 (**invited**).

- J. DiMaria, E. Dimakis, T. D. Moustakas, and R. Paiella, "Plasmonic collimation and beaming from LED active materials," IEEE Conference on Lasers and Electro-Optics, paper CF2E.2, San Jose (CA), June 2013.

- J. DiMaria, E. Dimakis, J. Henson, T. D. Moustakas, and R. Paiella, "Coupled metallic thin-film/nanoparticle-array systems for far-field engineering of quantum-well luminescence," IEEE Conference on Lasers and Electro-Optics, paper QTu2F.7, San Jose (CA), May 2012.

- J. Henson, E. Dimakis, J. DiMaria, T. D. Moustakas, and R. Paiella, "Diffraction-coupled plasmon-enhanced light emission from InGaN/GaN quantum wells," IEEE Conference on Lasers and Electro-Optics, paper CMU6, Baltimore (MD), May 2011.

- J. Henson, J. DiMaria, E. Dimakis, R. Li, S. Minissale, L. Dal Negro, T. D. Moustakas, and R. Paiella, "Plasmon-enhanced emission rates from III-nitride quantum wells using tunable surface plasmons," MRS Fall Meeting, paper M5.10, Boston (MA), Nov 2010.
- J. Henson, E. Dimakis, J. DiMaria, T. D. Moustakas, and R. Paiella, "Plasmon-enhanced light emission from InGaN quantum wells using lithographically defined nanoparticle arrays," IEEE Conference on Lasers and Electro-Optics, paper CTuNN1, San Jose (CA), May 2010.
- J. Henson, J. C. Heckel, E. Dimakis, J. Abell, G. Chumanov, T. D. Moustakas, and R. Paiella, "Plasmon-enhanced light emission from InGaN quantum wells using chemically synthesized silver nanoparticles," Frontiers in Optics / Laser Science Conference, paper FMH4, San Jose (CA), Oct 2009.
- J. Henson, J. DiMaria, and R. Paiella, "Tunable plasmonic resonances in two-dimensional arrays via nanoparticle height control," Frontiers in Optics / Laser Science Conference, paper FMA5, San Jose (CA), Oct 2009.
- J. Henson, A. Bhattacharyya, T. D. Moustakas, and R. Paiella, "Tunable surface-plasmon resonances in strongly coupled metallo-dielectric multiple layers," OSA Plasmonics and Metamaterials (META) Topical Meeting, paper MThC1, Rochester (NY), 2008.